Evaluation of the effect of sulfur on the performance of Ni/CGO-based solid oxide fuel cell (SOFC) anodes

Matthias Riegraf,[a,*] Vitaliy Yurkiv,[a] Rémi Costa,[a] Günter Schiller,[a] K. Andreas Friedrich[a]

Abstract: The focus of this paper is the measurement and understanding of sulfur poisoning phenomena of Ni/gadolinium-doped ceria (CGO) based solid oxide fuel cells (SOFC). Cells with Ni/CGO10 and NiCu5/CGO40 anodes were characterized by means of impedance spectroscopy at different temperatures and H_2/H_2O fuel ratios. The short-time sulfur poisoning behavior was systematically investigated for varying temperatures of 800 – 950 °C and current densities of 0 – 0.75 $A{\cdot}cm^{-2}$ with H_2S concentrations between 1 – 20 ppm. A sulfur poisoning mitigation effect was observed at high current loads and temperatures. The poisoning behavior was shown to be reversible for short exposure times. It was observed that the sulfur-affected processes exhibited significant different relaxation times depending on the Gd content in the CGO phase. Moreover, it was demonstrated that the capacitance of Ni/CGO10 anodes is strongly dependent on temperature and gas phase composition reflecting a changing Ce^{3+}/Ce^{4+} ratio.

Introduction

Over the last few decades, the challenges associated with global warming and the progressing depletion of natural resources have sparked increasing interest in the development of highly efficient electrochemical energy devices that allow the use of a variety of renewable fuels such as hydrogen, syngas or biogas. In this context, due to their high operating temperatures giving rise to fast electrode reaction kinetics, solid oxide fuel cells (SOFC) are a promising technology since they are able to readily convert hydrocarbons, CO and biofuels without the necessity of employing noble metals as catalysts.[1] However, both biogas and natural gas usually contain undesirable sulfur-containing species that lead to the poisoning of Ni-containing fuel electrodes entailing significant SOFC performance decrease within a short period of time. Sulfur poisoning of the commonly used Ni/YSZ cermet anodes has been widely investigated, both experimentally and theoretically.[2–7] However, in comparison to Ni/YSZ, fewer studies on the sulfur poisoning behavior of Ni/CGO anodes exist in literature although they showed a significantly higher sulfur tolerance than Ni/YSZ.[8–15] Thus, hitherto the underlying microscopic processes defining the performance characteristics and the sulfur poisoning behavior of Ni/CGO electrodes have not been fully understood.

Recent studies on electrochemical reactivity of Ni/CGO anodes have observed fundamental differences to Ni/YSZ in the fuel oxidation mechanisms.[16–18] Hence, in order to explain the high sulfur resistance of Ni/CGO, an advanced understanding of the fuel oxidation mechanism is required. The present state of knowledge is briefly reviewed in the following section.

[a] M. Riegraf, Dr. V. Yurkiv, Dr. R. Costa, Dr. G. Schiller, Prof. Dr. K. A. Friedrich
Institute of Engineering Thermodynamics
German Aerospace Center (DLR)
Pfaffenwaldring 38-40, 70569 Stuttgart, Germany
E-mail: matthias.riegraf@dlr.de

Supporting information for this article is given via a link at the end of the document.

Background

Fuel oxidation mechanism on Ni/doped ceria anodes

While the drastic performance decrease of SOFC with Ni/YSZ anodes was shown to be related to the Ni surface poisoning with elemental sulfur, recent fundamental studies of Ni/CGO anodes have observed the electrochemistry to take place on the CGO rather than on the Ni surface. Thus Ni was suggested to act primarily as electronic conductor.[16–18] At common SOFC operating conditions (temperatures above 700 °C and under reducing atmosphere), CGO displays high surface activity towards H_2 and CH_4 oxidation and mixed ionic and electronic transport properties due to the mixed oxidation state of cerium which can easily hop between Ce^{3+} and Ce^{4+}. This phenomenon could extend the electrochemical reaction zone in the composite electrodes from the triple phase boundary (TPB) to the double phase boundary interface between ceramics and gas (2PB).[8,13,16,17,19–23] Thus, the spillover of reaction intermediates at the triple phase boundary (TPB) between ceramic and metallic phase that occurs in Ni/YSZ anodes is likely not the rate-limiting step during hydrogen oxidation on Ni/CGO.[16,17,21–23] Recently, it was suggested that hydrogen oxidation proceeds via an OH^- intermediate that binds to the surface vacancies.[19] The adsorption of hydrogen and water on the surface oxygen vacancies was experimentally observed to be very fast and hence, can be assumed to be quasi-equilibrated. In this context, the electron transfer between the OH^- intermediate and Ce^{4+} was suggested to be the rate-determining step in the hydrogen oxidation process. Using impedance spectroscopy on symmetrical cells, several studies have reported two distinct contributions in the spectra of Ni/CGO anodes both of which are ascribed to actual electrode processes.[22,24–27] The capacitive nature of at least one of these processes was related to a surface double layer. Such capacitance is frequently observed in MIEC electrodes and is caused by the accumulation of electronic charges in the space-charge layer of the MIEC surface and adsorbed ions on the surface. [28–30]

While, the process at middle frequencies (20 – 100 Hz) was recently interpreted to represent the electrochemical oxidation of hydrogen including charge transfer,[22,27,31] other studies assigned this impedance feature to oxide ion transport in the

MIEC itself or across the electrolyte/MIEC interface.[22,24] Regarding the process at lower frequencies (0.1 – 10 Hz), no definite assignment has been achieved so far. It has been shown to be dependent on the active surface area of the doped ceria phase and was therefore assigned to a surface process. Hydrogen adsorption coupled to surface diffusion on CGO was suggested as well.[21,24,25] The described studies partly employ electrodes with different Gd-doping contents between 10 – 40 %. The demonstrated different interpretations of the observed impedance processes give rise to the assumption that the different Gd doping levels could entail fundamental differences in the cell behavior.

Sulfur poisoning of Ni/CGO anodes

Several research groups have experimentally investigated the influence of sulfur-containing fuels on Ni/CGO-based SOFC performance.[8–15] However, there is significant discrepancy between these studies concerning the interpretation of the results. In most cases, a rapid initial power output drop occurs already for H_2S concentrations in the ppm level with an accompanying increase in total anode resistance. Upon poisoning with 2 ppm H_2S, Schubert et al. have observed a power output drop of less than 2 % and a full recovery after switching off the H_2S supply.[8] Moreover, Aravind et al. have not witnessed any effect at all on impedance spectra after sulfur poisoning with 9 ppm H_2S.[11] In studies investigating the influence of higher hydrogen sulfide concentrations, the formation of Ce_2O_2S was observed.[32] However, ceria and Ni were shown not to form any bulk sulfide phases at H_2S concentrations higher than 100 ppm.[33] A few studies have directly compared sulfur poisoning of Ni/CGO and Ni/YSZ anodes, and observed the poisoning behavior to be remarkably similar as the saturation of the resistance increase levels off with increasing H_2S concentration in the same manner for both anodes. Consequently, sulfur poisoning of Ni/CGO anodes has frequently been interpreted under the assumption that the underlying mechanism is the same as for Ni/YSZ and therefore has not yet been the subject to the same detailed analysis. While the performance drop upon sulfur exposure of SOFC with Ni/YSZ anodes was related to the sulfur surface blockage of Ni, this is unlikely to have an influence on Ni/CGO anodes with Ni as a pure electronic conductor, leaving the real impact of sulfur unclear. Recently, it has been reported that pure CGO anodes without the presence of a metallic phase also suffer from sulfur poisoning under exposure to 10 ppm H_2S demonstrating the possibility of sulfur adsorption on the ceramic and the corresponding active surface blockage.[34] The possible sulfur poisoning of ceria surfaces at high temperatures was further demonstrated by Mullins et al. using temperature-programmed desorption (TPD) experiments combined with soft X-ray photoelectron spectroscopy (sXPS). The authors investigated the H_2S exposure of reduced CeO_2(111) surfaces showing that hydrogen sulfide dissociates on the surface vacancies to OH and SH and further into elemental sulfur.[35] Depending on the extent of ceria reduction, they showed that either H_2 or H_2O desorb at about 600 K while sulfur remains on the oxygen surface vacancy sites at higher temperatures. However, the authors indicated that above 800 K sulfur could diffuse into the bulk phase of ceria. Besides that, they could not detect any SO_x products in the exhaust gas.[35]

In order to shed more light on the sulfur poisoning process of Ni/CGO anodes, in the present work the impact of hydrogen sulfide on Ni/CGO10 and Ni/CGO40-based anodes is systematically investigated for the varying parameters temperature, current density and H_2S concentration. Subsequently, this impact is evaluated taking into account recent findings from literature giving insight into the corresponding fuel oxidation mechanism.

Results and Discussion

A main objective of the present study is to establish the influence of sulfur poisoning on Ni/CGO-based anodes. Therefore, two kinds of Ni/CGO anodes with different Gd doping levels are studies. However, prior to the detailed investigation of the poisoning phenomena, a fundamental understanding of the fuel oxidation mechanism on CGO based anodes is necessary. For that reason, the general approach is to compare different electrochemical measurements employing two types of anodes (cell A and cell B) towards electro-catalytic reactivity without and with sulfur containing fuels. Thus, this manuscript firstly presents the extensive characterization of the cells in non-sulfur systems and subsequently the sulfur poisoning behavior of the investigated cells.

Identification of physico-chemical processes in non-sulfur systems

Ni-CGO10-based cell

Figure S3 reports *i-V* curves of cell A in H_2/H_2O (97/3) mixture and stepwise varying temperatures from 650 °C to 950 °C. The current density at 0.7 V reaches 0.93 $A \cdot cm^{-2}$ at 850 °C demonstrating high performance of the cell. Figure 1a shows the Nyquist plot of impedance spectra measured at different operating temperatures and Fig. 1b the corresponding imaginary impedance plot. Analogously, Figs. 1c+d depict Nyquist and imaginary impedance plots for different humidity levels at 850 °C. The Nyquist plots at higher temperatures clearly show two separated arcs as it is also commonly observed for SOFC with Ni/YSZ anodes. Fig. 1b shows that the peak frequency of the middle-frequency arc lies at approximately 200 Hz at 850 °C, while the low-frequency peak is at approximately 0.2 Hz. With decreasing temperature the middle frequency contribution can be further distinguished into two peaks. For example, at 700 °C one contribution is visible at about 35 Hz and another one at 5 Hz. Both contributions show thermal activation and thus, can be interpreted as physico-chemical electrode processes.

Figures 1a+b show also a temperature dependency in the low-frequency region indicating the existence of a thermally activated electrode process in addition to a gas conversion process that is expected to have only a small temperature-dependency.[36,37] With decreasing temperature, the peak

frequency of the low-frequency contribution shifts to higher frequency values between 750 °C and 650 °C. This is an uncommon behavior for thermally activated processes, which usually exhibit a peak shift to lower frequencies caused by an increase in resistance under these conditions. Consequently, the observed behavior must be caused by a significant decrease of capacitance with decreasing temperature, according to the relationship $f_S = 1/(2\pi RC)$ with R being the process resistance, f_S the peak frequency and C the capacitance. This change in capacitance will also be further discussed in the following sections. At temperatures higher than 800 °C, the peak frequency and peak intensity stay constant indicating a less temperature-dependent behavior of the low frequency arc in this region. This could suggest that at higher temperatures, the gas conversion dominates the low frequency arc, while at lower temperatures the physico-chemical anode process prevails. In the present study, thin anodes (<30 µm) are employed, therefore resistances due to porous transport are negligible.[38]

Increasing pH$_2$O primarily leads to a strong reduction of the low-frequency contribution in the impedance spectra at a frequency range between 0.1 and 1 Hz as depicted in Figs. 1c+d. While this is to be expected for gas conversion, the strong reduction of the peak also suggests an enhancing effect of increasing water partial pressures on the kinetics of the low frequency process. This suggests the origin to be an anode surface process as it was already observed in symmetrical cell measurements of Ni/CGO10 anodes at similar frequencies.[26,27,39] The middle-frequency contribution of the impedance spectra at frequencies greater than 100 Hz is not affected by changing pH$_2$O indicating the absence of a surface anode process in this region.

As shown in the supplementary information in Fig. S3, the replacement of the air supply with pure oxygen at 850 °C leads to a reduction of the middle frequency peak mainly at a frequency range of approximately 50 to 100 Hz. This confirms the existence of a cathode surface process in this region, which is also in accordance with literature studies of LSM/YSZ cathodes.[40–42] However, the reduction of the cathode contribution in the impedance spectra still leaves a significant middle peak contribution in the impedance spectra at a frequency of about 200 Hz indicating the existence of another anode process in this region. This is consistent with literature studies on symmetrical Ni/CGO cells that show one middle and one low-frequency contribution.[24,27] While these studies report the low-frequency contribution to be dependent on the anode gas phase composition, the middle-frequency process was not affected, thus giving rise to its ascription to an anode bulk process. The origin of this middle-frequency bulk process was suggested to be the oxide ion transport from bulk to surface or across the electrolyte/anode interface.[24,25] The low frequency contribution is excluded to be due to gas diffusion since the corresponding process was reported to be thermally activated.[24,27] Primdahl et al. rather attributed this process to hydrogen adsorption and dissociation, possibly connected with a surface diffusion process since they observed a considerable resistance decrease upon the addition of a small catalytic amount (0.8 wt %) of nickel.[25] Moreover, the process showed an isotope mass effect as it would be expected from hydrogen adsorption and dissociation.[24]

As a summary, two processes could be identified in the impedance spectra of cell A. One middle-frequency process is not affected by humidity, thus, is ascribed to a bulk process. Additionally, one low-frequency process was shown to be pH$_2$O dependent, hence, it is attributed to a surface process.

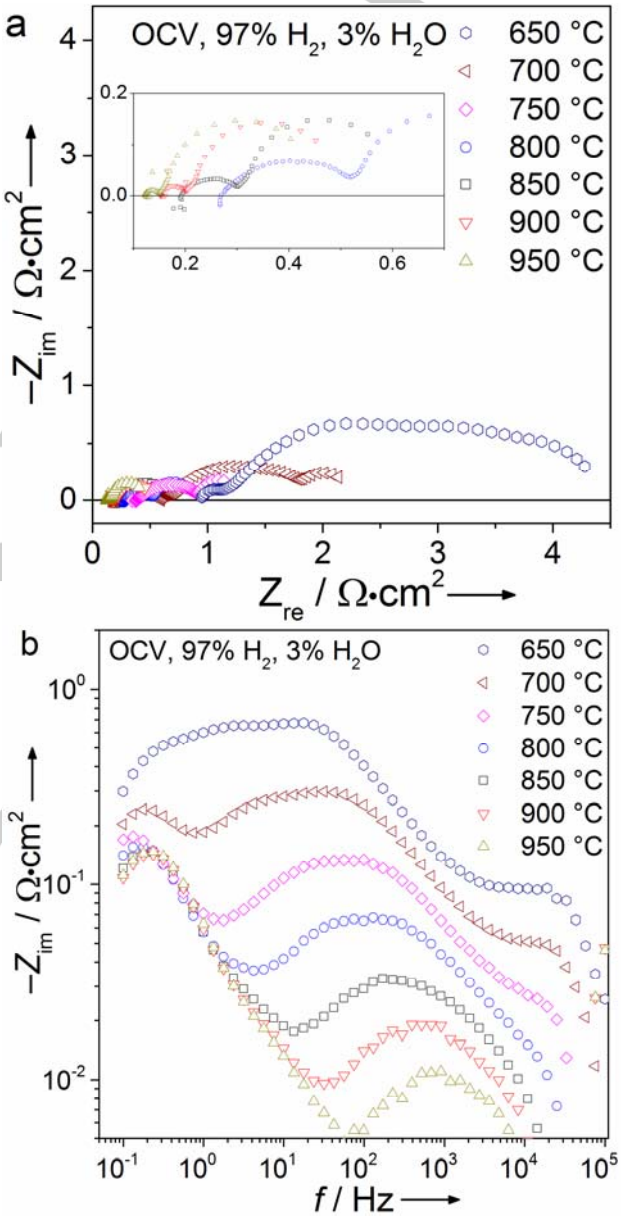

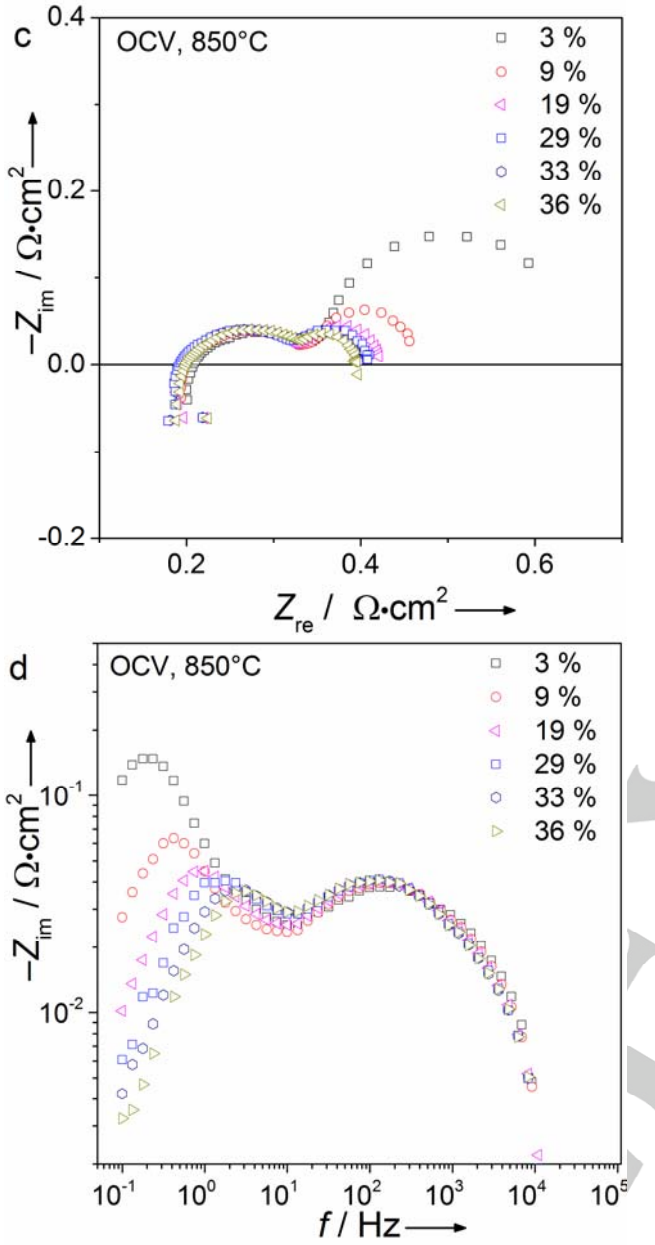

Figure 1. (a) Nyquist and (b) imaginary impedance plot of impedance spectra of Ni/CGO10-based SOFC measured at different temperatures T = 650 °C – 950 °C, OCV, pO_2 = 0.21 atm, pH_2 = 0.97 atm, pH_2O = 0.03 atm, (c) Nyquist and (d) imaginary impedance plot of impedance spectra measured at T = 850 °C, OCV, pO_2 = 0.21 atm, varying pH_2O = 0.03 – 0.36 atm.

Ni/CGO40-based cell

Figure S4 depicts i-V curves of cell B. The current density at 0.7 V reaches more than 0.5 A·cm^{-2} at 800 °C and thus, compared to 0.62 A·cm^{-2} at 800 °C for cell A, the performance of cell B is slightly lower. Figure 2a shows the Nyquist plot of impedance spectra measured at different operating temperatures between 700 – 950 °C and Fig. 2b the corresponding imaginary impedance representation. Analogously, Figures 2c+d show Nyquist and imaginary impedance plots for different pH_2O at 850 °C. In the Nyquist plots two clearly separated arcs can be distinguished. Fig. 2b illustrates that the peak frequencies of the high-frequency arc lie between 10^1 and 10^2 Hz at common ESC operating temperatures above 800 °C. Although it has to be noted that there is also a cathode process present at frequencies of about 50 Hz (depicted in Fig. S5), the influence of changing water partial pressure at 10^1 – 10^2 Hz on the imaginary impedance plot in Fig. 2d clearly indicates the existence of an anode surface process. The intensity of the peak of this anode process is lowered and its characteristic frequency peak is slightly shifted to higher values with increasing pH_2O, reflecting the decreasing process resistance caused by enhanced kinetics. Although this seems to be counter-intuitive, a similar enhancing effect of increasing pH_2O on H_2 oxidation kinetics has already been observed for Ni/YSZ anodes caused by the participation of H_2O as reactant in one of the rate-limiting steps.[43] This indicates a similar role of H_2O in the oxidation mechanism of Ni/CGO40-based anodes.

The existence of an anode surface process at approximately 100 Hz is contrary to the results shown in Fig. 1d for a Ni/CGO10-based cell, which did not show a significant influence of water in this frequency range. This gives rise to the assumption that the same anode surface process appears in completely different frequency ranges for the different cells. In symmetrical cell measurements of Ni/CG40 anodes with a similar design as in the present study, Iwanschitz et al. observed two anode processes, one middle frequency process between 50 – 100 Hz and one low frequency process at 1 – 2 Hz.[22] While they admit that gas conversion could contribute to the low-frequency process, based on the observation that redox cycling was observed to have an effect on this process and a comparison to other literature sources, they interpreted it as an actual electrode process rather than a gas transport process. Upon a decrease of temperature in Figure 2, a small effect on the low-frequency impedance spectra is visible by a peak shift to higher frequencies at 750 °C. However, the increase of pH_2O in the fuel gas leads to a stepwise decrease of the intensity of the low frequency peak in Fig. 2d, displaying the typical behavior of a gas conversion process. At a humidity level of 0.3 atm, the low frequency peak has nearly disappeared. In order to better deconvolute the gas conversion and the low-frequency anode process observed in literature, the fuel gas flow rate was decreased from 1 l•min^{-1} to 0.2 l•min^{-1}. Additionally, at this comparatively low specific fuel gas flow rate the pH2O was varied between 0.15 and 0.5 atm. The impedance spectra recorded at the respective operating conditions are shown in Fig. 3. Both the Nyquist plot in Fig. 3a and the imaginary impedance plot in Fig. 3b indicate the presence of more than one semi-circle in the low-frequency arc pointing towards the existence of another low-frequency process in addition to gas conversion. This is further confirmed by the calculated DRT in Fig. 4c that shows the existence of one process at 0.3 Hz and another one at 0.02 Hz at 0.15 atm, both of which exhibit a dependency on the humidity content. This underlines the difficulties associated with their assignment to a specific process. However, as a reduction of the fuel gas flow rate generally results in a shift of the gas conversion process to lower frequencies, the process at 0.02 Hz is suggested to be due to

gas conversion. This implies that the process at 0.3 Hz is an anode process as suggested by Iwanschitz et al.[22] In the present study, the same anode design was used as in the work by Iwanschitz et al., except for the addition of small amounts of Cu in the metallic phase. The observation of anode processes at the same frequency in the impedance spectra is strong evidence that the influence of Cu on the hydrogen oxidation mechanism is indeed negligible. However, alloying Ni with Cu has shown to lower the sulfur adsorption energy for $Ni_{0.5}Cu_{0.5}$.[44,45] Thus, although the amount of Cu in the present study is much smaller, a minor influence of Cu on the magnitude of the sulfur poisoning-related resistance increase cannot be excluded.

As a summary, two low frequency processes could be identified in the impedance spectra of cell B as well. However, in contrast to cell A, the middle-frequency process is affected by humidity, and therefore is assigned to a surface process. Additionally, one low-frequency process with unclear origin was observed. No bulk anode process in the middle-frequency range was observed, however, due to possible convolution of processes in this region, its existence cannot be excluded.

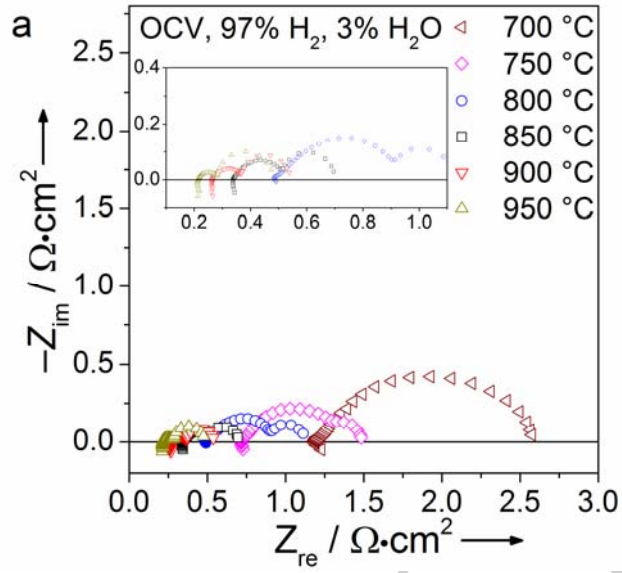

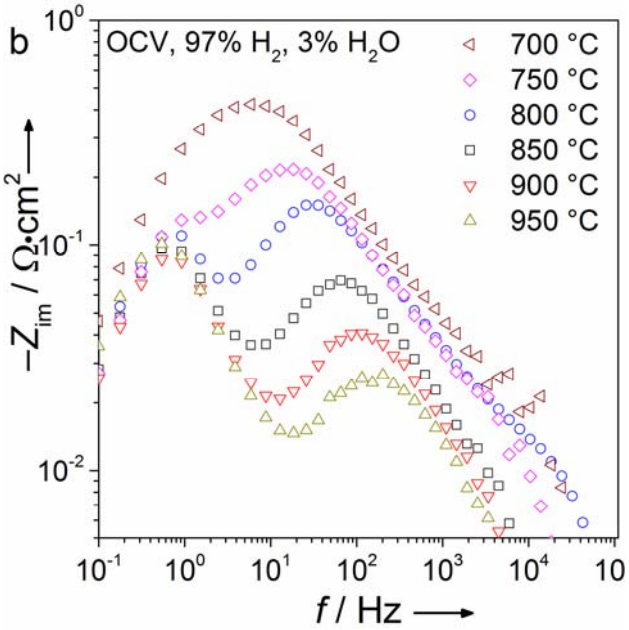

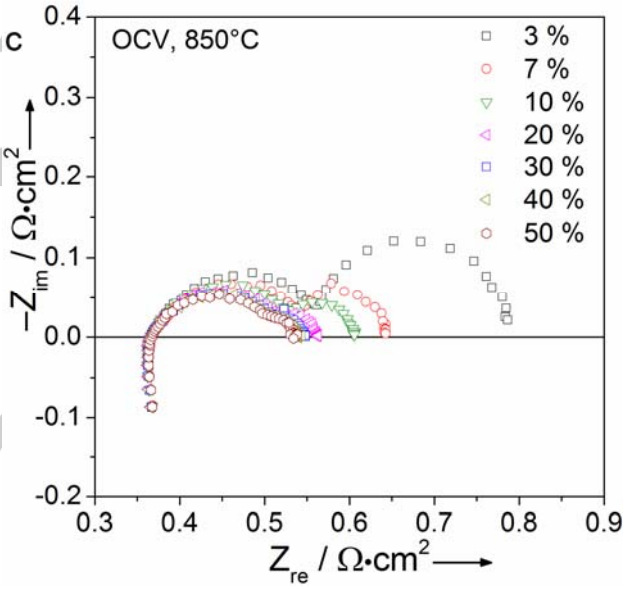

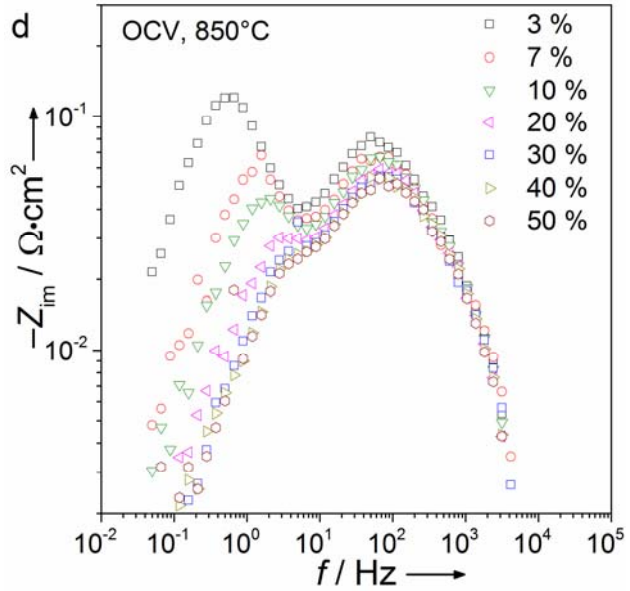

Figure 2. (a) Nyquist and (b) imaginary impedance plot of impedance spectra of a Ni/CGO40-based SOFC recorded at different temperatures T = 700 °C – 950 °C, OCV, pO_2 = 0.21 atm, pH_2O = 0.03 atm, (c) Nyquist and (d) imaginary impedance plot of impedance spectra of the cell recorded at T = 850 °C, OCV, pO_2 = 0.21 atm, varying pH_2O = 0.03 – 0.5 atm.

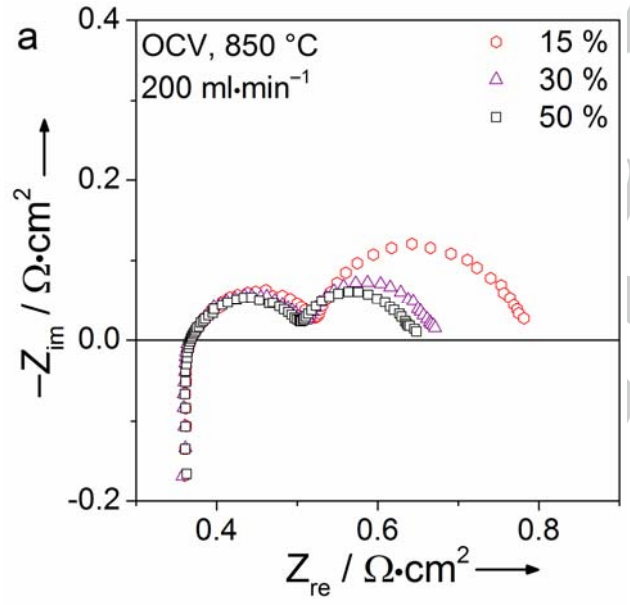

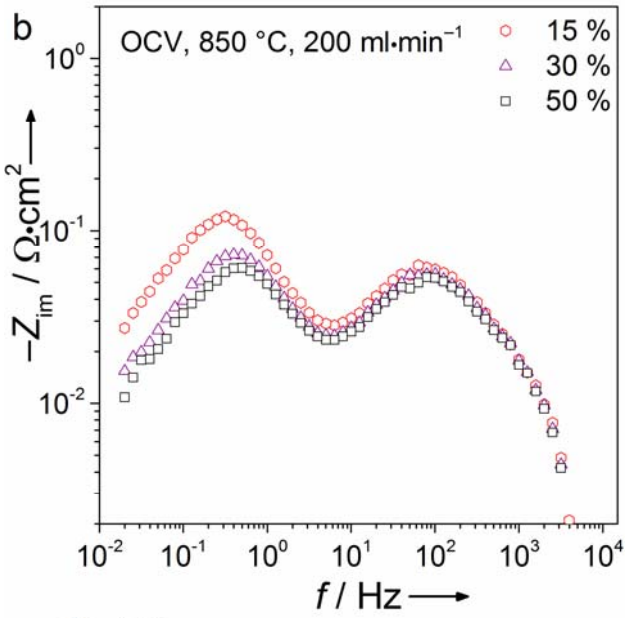

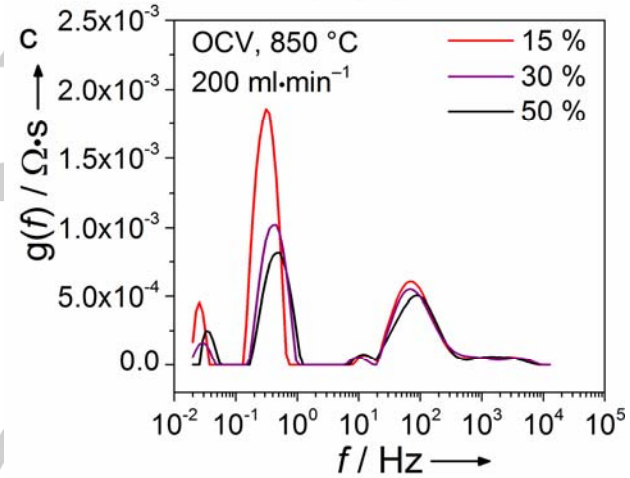

Figure 3. (a) Nyquist and (b) imaginary impedance plot of impedance spectra of a Ni/CGO40-based SOFC recorded at T = 850 °C, OCV, pO_2 = 0.21 atm, 200 ml•min^{-1} with varying pH_2O = 0.15 – 0.5 atm. (c) shows the calculated distribution of relaxation times (DRT).

Sulfur Poisoning

In the following subsection, the systematic investigation of sulfur poisoning of the two different anodes is presented. In order to facilitate the comparison of each cell's poisoning behavior at the different operating conditions, all sulfur poisoning experiments were conducted with the same cell, as this approach avoids problems regarding slightly different performance, tightness and contacting. As the sulfur poisoning behavior on Ni/CGO anodes is expected to be mainly reversible, this approach should be viable as shown in the following. In order to avoid sulfur-related irreversible degradation, after saturation of the respective performance drop was reached, the poisoning intervals were kept as short as possible.

Sulfur poisoning of Ni-CGO10-based anodes

In Fig. S6, the voltage stability tests over time are depicted at all conditions for temperature variations between 800 °C and 900 °C and current density variations at constant T = 850 °C between OCV and 0.75 A·cm^{-2}. In all cases, the overall voltage drop is stepwise increasing along with the H_2S concentration. The initial performance drop associated with the exposure of 1 ppm is the largest while the further increase of H_2S concentration only leads to smaller performance losses. For the exposure times investigated in the present study, full recovery was reached within 22 hours after switching off the sulfur supply at all operation points.

Since the introduction of hydrogen sulfide did not lead to a voltage drop at OCV, the poisoning characteristics were captured with impedance spectroscopy. The corresponding recorded spectra are illustrated in Figure 4. While sulfur exposure has no influence on the identified bulk processes in the middle frequency region, it leads to an increase in the low-frequency arc associated with an influenced frequency range around about 0.1 Hz, which is consistent with the identification of an anode surface process at this frequency in Fig. 1. This value is approximately 4 orders of magnitude lower than the peak frequencies commonly observed for Ni/YSZ-based SOFC (~10^3 – 10^4 Hz) that display an electric double layer capacitance at the interface between electrolyte (YSZ) and electrode (Ni).[2,6,46] Thus, due to the large shift in relaxation frequency it can be concluded that the capacitance of the observed Ni/CGO10 anode process has a different nature than the one for Ni/YSZ anodes indicating fundamental differences in the underlying hydrogen oxidation mechanisms. The low frequency of the observed anode surface process is in good agreement with the frequency of Ni/CGO10 electrode processes reported in literature.[24,39] Furthermore, the low frequency surface process is consistent with reports of the frequencies of nickel-free CGO10 and CGO20 electrodes.[21]

In these studies, the nature of the low-frequency process was related to hydrogen oxidation on the CGO surface causing a surface/gas phase double layer, which leads to an electrostatic potential step between surface and bulk. It was shown that Gd-doped ceria is characterized by the occurrence of a chemical capacitance similar to other mixed ionic electronic conductors.[47,48] At the MIEC surface, a double layer is created by the accumulation of electronic charges in the space-charge layer near the MIEC surface (here: Ce^{3+}) and ions being adsorbed on the surface (here: OH^-).[29] Thus, a changing electrode potential is reflected by a simultaneous change in

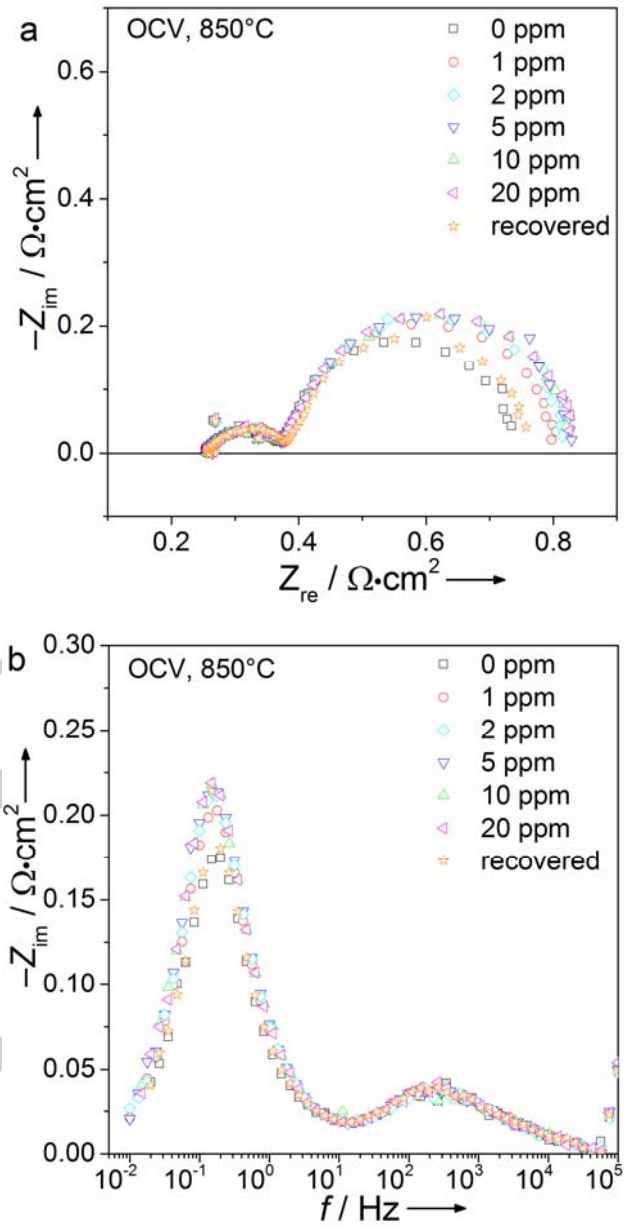

Figure 4. a) Nyquist and (b) imaginary impedance plot of impedance spectra of cell A recorded at temperature T = 850 °C, OCV, pO_2 = 0.21 atm, pH_2 = 0.97 atm, pH_2O = 0.03 atm, with different H_2S concentrations between 0 – 20 ppm.

concentration of the electrochemically relevant adsorbants and Ce^{3+}/Ce^{4+} ratio as a result of the following global reaction:

$$2\,Ce_{Ce}^{x} + O_O^x + H_2 \rightleftharpoons 2\,Ce_{Ce}^{'} + V_O^{\bullet\bullet} + H_2O \qquad (i)$$

where the species in the Kröger-Vink notation are Ce^{4+}, O^{2-}, Ce^{3+} and the oxygen vacancy from left to right. Feng et al. investigated samaria-doped ceria (SDC20) at 500 °C and proposed the electron transfer between the OH^- intermediate and Ce^{4+} to be the rate-limiting step that can be expressed as:

$$Ce_{Ce}^{'} + OH_O^{\bullet} \rightleftharpoons Ce_{Ce}^{x} + OH_O^x \qquad (ii)$$

where $OH^{\bullet}_{O}$ sits on the surface oxygen vacancy site.[19] Thus, surface reduction leads to an increasing number of oxygen vacancies on the surface and a higher Ce^{3+} concentration.[49] Thus, the mixed valent Ce^{3+}/Ce^{4+} are responsible for the large chemical capacitance. This capacitance, in turn, could possibly be coupled to hydrogen dissociation on Ni explaining the low frequency influence of sulfur poisoning.

The influence of current density and temperature.

Recent studies on sulfur poisoning of Ni/YSZ have demonstrated the difficulties of finding an appropriate descriptor in order to quantify the extent of sulfur poisoning in full cell measurements as cathode and gas diffusion/concentration resistance contributions might superimpose the anode poisoning behavior.[5,50,51] As it was not possible to deconvolute the anode surface process from the gas conversion process at low frequencies in order to calculate the relative resistance increase upon poisoning, in the present study we have employed the absolute decrease in voltage and the absolute increase of total area-specific cell resistance (ASR) in order to evaluate the extent of sulfur poisoning. The values of the voltage drops in Fig. 5a show the same characteristic behavior for all current densities with a sharp drop for low H_2S concentrations and a saturation effect at higher concentrations. This strongly resembles the saturation effect also observed for Ni/YSZ which was related to the saturation of S on the Ni surface.[2,52,53] The sulfur coverage on Ni can be estimated by means of a Temkin isotherm as shown by Alstrup et al. [54] The respective calculated values for the conditions employed in the present study are depicted on the right y-axis in Fig. 5a. The behavior of sulfur coverage on Ni and the voltage drop is indeed strikingly similar, indicating that the observed Ni/CGO sulfur poisoning could be due to Ni surface poisoning. This is consistent with literature studies reporting that Ni infiltration enhances the same low frequency process as sulfur poisoning of CGO slows down.[25,34] Contrary to earlier reports on sulfur poisoning of Ni/CGO anodes, the voltage drops in the present study demonstrate that sulfur poisoning of Ni/CGO-based anodes can affect SOFC performance significantly.[8,10,11] The comparison of the different curves in Fig. 5 reveals that increasing current densities lead to higher drops in performance. Whereas this behavior itself is not surprising, the increase of ASR in Fig. 5b shows the opposite behavior indeed indicating some kind of mitigation effect at high current densities. However, interestingly the ASR increase values for the experiments at OCV are not in accordance with this trend since they are significantly smaller than the ASR increase values for 0.25 $A \cdot cm^{-2}$. While we cannot explain this behavior, we would like to note that it could be reproduced with different cells of the same type.

Previous investigations of sulfur poisoning of Ni/YSZ anodes revealed that the relative increase in ASR tends to decrease with increasing polarization, giving rise to the hypothesis that large oxygen ion flows lead to a reduced sulfur surface coverage on Ni via a S oxidation reaction to SO_2.[50] However, recent studies have shown the contrary behavior.[2,5,7] Thus, the observed mitigation effect might be related to improved anode kinetics due to increased humidity levels in the anode compartment rather than to an actual sulfur oxidation to SO_2 and the subsequent removal from the anode surface. Furthermore, the fact that the values of ASR increase for the OCV experiment are lower than the one for an applied current density of 0.25 $A \cdot cm^{-2}$ is inconsistent with the hypothesis of SO_2 formation. Nonetheless, we would like to point out that recent density functional theory (DFT) calculations of sulfur oxidation on doped ceria surfaces showed that sulfur oxidation to SO_2 displays favorable kinetics as surface lattice oxygen could be used to oxidize the ceria-adsorbed sulfur.[55]

Both Fig. 5c and 5d show the same trend of a lower voltage drop, respectively lower ASR increase with increasing temperature, indicating a mitigating effect of temperature on the extent of sulfur poisoning. A similar behavior has also already been observed for sulfur poisoning of Ni/YSZ and was related to an increasing desorption of H_2S from the Ni surface with increasing temperature and thus, a reduced sulfur surface coverage.[56] This could also be the case in the present study, as desorption processes are generally endothermic and hence, energetically more favorable with increasing temperature.

The observed voltage drops for higher H_2S concentrations at 800 °C reach values of over 100 mV. These voltage drops already approach the magnitude of values observed for Ni/YSZ.[52] This is a lot more severe compared to what earlier studies have reported for Ni/CGO10 anodes.[8,10] The reason for the significantly larger performance drops in the present study are so far unclear. However, they indicate that the microstructure of Ni/CGO anodes plays an important role in determining the sulfur tolerance of such electrodes.

The differential impedance spectra in Fig. 6a confirm the behavior observed in Fig. 5d with a more pronounced increase of the imaginary impedance at higher temperatures after exposure of the anode to 1 ppm H_2S. Interestingly, however, the peak frequency of the differential impedance spectra increases with decreasing temperature, implying the characteristic frequency of the low-frequency anode surface process to change as well. As already indicated earlier, this is rarely observed for SOFC, as thermally activated processes generally exhibit higher resistances at lower temperatures causing the corresponding characteristic frequencies to shift to lower values. Hence, the observed behavior must be caused by a significant decrease of capacitance with decreasing temperature. This is also confirmed by the results of a complex nonlinear least-squares (CNLS) fit of a reduced equivalent circuit model (ECM) to the experimental data. The ECM is depicted in Fig. S7 and the corresponding results are shown in Table S1.

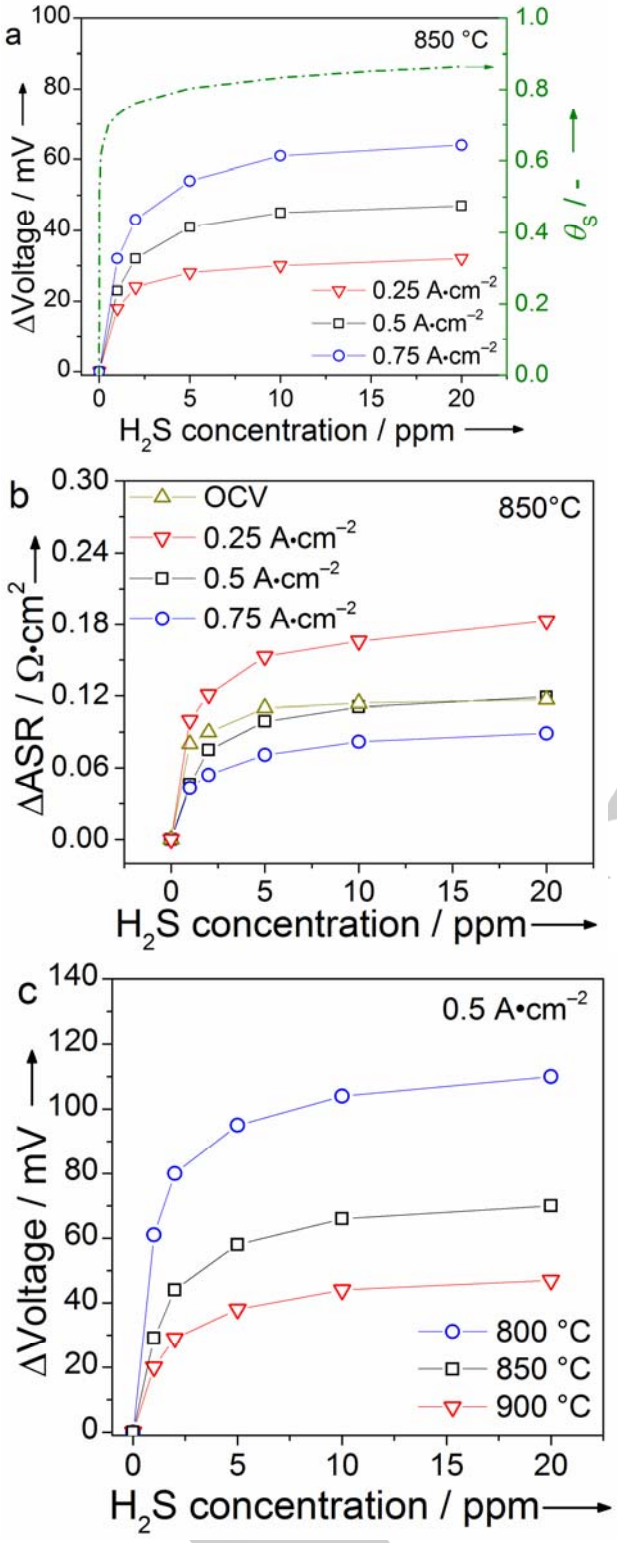

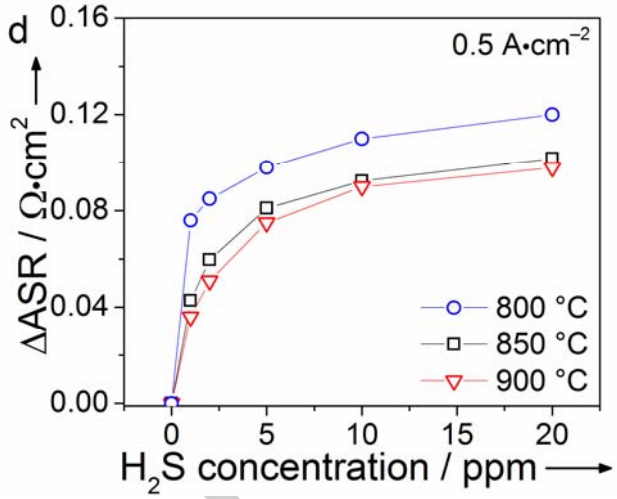

Figure 5. (a) Accumulated voltage drop and (b) accumulated total resistance increase at temperature T = 850 °C, pO$_2$ = 0.21 atm, pH$_2$ = 0.97 atm, pH$_2$O = 0.03 atm, as a function of H$_2$S concentration at different current densities. (c) Accumulated voltage drop and (d) accumulated ASR increase at a current density of 0.5 A·cm^{-2}, pO$_2$ = 0.21 atm, pH$_2$ = 0.97 atm, pH$_2$O = 0.03 atm, as a function of H$_2$S concentration at temperatures. The right y-axis in a) shows the calculated sulfur coverage on Ni according to the Temkin isotherm derived in Ref.[54]. As mentioned earlier, the experiments in (c) and (d) were conducted with a different cell from the same batch as the cell in (a) and (b). Thus, the values do not coincide completely.

Similar analysis can be made based on the differential impedance spectra for varying current densities depicted in Fig. 6b. The peak intensities confirm the trends observed in Fig. 5b, with the test at 0.25 A·cm^{-2} being the most severely poisoned by 1 ppm H$_2$S. Again, it is interesting to see that the increase in current density leads to a peak frequency shift from 0.1 Hz at OCV to 1.4 Hz. While a certain shift to higher frequencies can be expected due to the possibly accelerated kinetics at higher pH$_2$O, a shift of more than one order of magnitude is comparatively large.[57] Although it is well-known that double layer capacitances can be dependent on temperature and gas composition,[58] this influence is negligible in many cases and they are frequently assumed to be constant.[38,59] However, the present results suggest that the chemical capacitance of the surface anode process leading to hydrogen oxidation on Ni/CGO10 is highly dependent on both parameters. As already mentioned, the chemical capacitance of the anode surface process is due to the mixed valent Ce^{3+}/Ce^{4+}. Recently, it has been shown that the Ce^{3+} surface concentration in CGO is almost independent of temperature and oxygen activity, however, Ce^{3+} bulk concentration considerably increases with increasing temperature and decreasing pO$_2$, which is consistent with the capacitance changes observed in the present work.[18,20,60] This could indicate that the chemical capacitance for Ni/CGO10 is not only constrained to the surface, but further extended into the bulk.

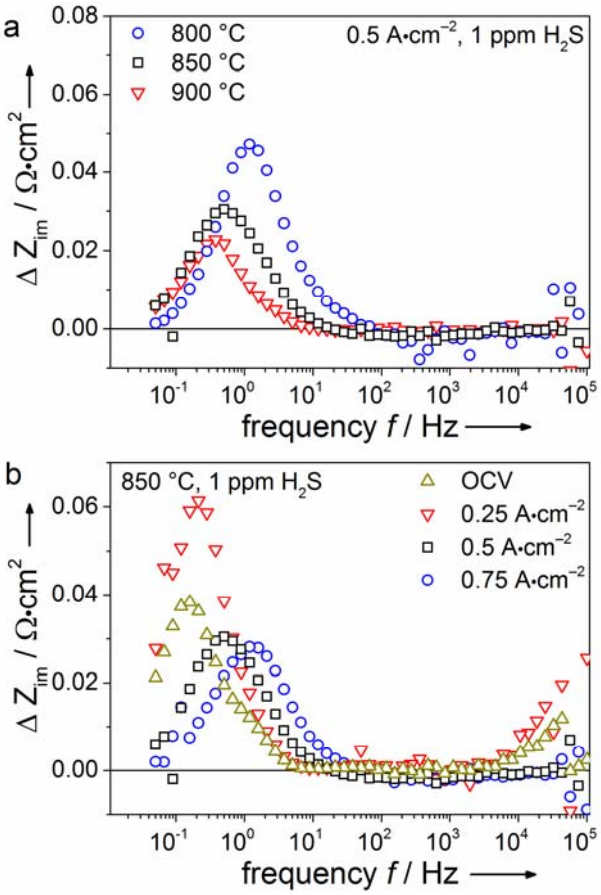

Figure 6. Differential impedance spectra (subtraction of imaginary impedance of 0 ppm H_2S spectra from 1 ppm H_2S) for a) different temperatures at constant i = 0.5 A·cm^{-2} and b) different current densities at constant T = 850 °C.

Sulfur poisoning of Ni/CGO40-based anodes

In the following, electrochemical results for sulfur poisoning of cell B are presented with a systematic variation of current density and temperature as described earlier. All sulfur poisoning experiments are shown in Fig. S8. The overall poisoning behavior of cell B strongly resembles the one of cell A with a significant voltage drop after exposure to 1 ppm H_2S and a subsequent saturation of the voltage drop. However, while the regeneration of cell B between 850 and 950 °C leads to a complete voltage recovery at all operating conditions, this is not the case for 800 °C (Fig. S8b). At this operating temperature, the voltage stabilizes after approximately 20 h of poisoning, but at a value 10 mV lower than the initial one. This demonstrates that sulfur exposure can also cause irreversible degradation on Ni/CGO anodes. As this irreversible degradation behavior could not be observed at any other operation point and the investigation at 800°C was conducted last in the present study, the most likely explanation for this behavior is that the onset of irreversible degradation is only reached after a certain time of operation. More carefully planned long-term experiments under varying conditions will be required in order to confirm this hypothesis.

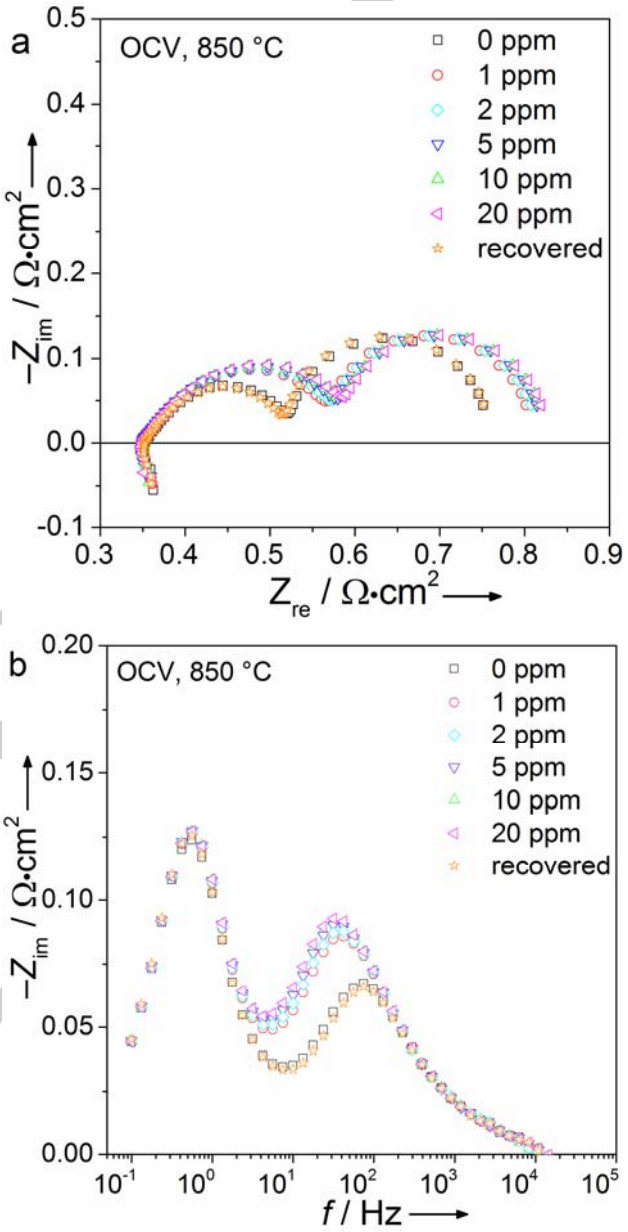

Figure 7. a) Nyquist and (b) imaginary impedance plot of impedance spectra of cell B recorded at temperature T = 850 °C, OCV, pO2 = 0.21 atm, pH2 = 0.97 atm, pH2O = 0.03 atm, with different H2S concentrations between 0 – 20 ppm.

Fig. 7 shows that impedance spectra at OCV are affected by sulfur exposure by means of an increase of the higher-frequency arc in the Nyquist plot at a frequency range between 10^1 and 10^2 Hz. The plots of the initial and the recovered impedance spectra overlap at each recorded frequency point, indicating a full recovery also at OCV. The low-frequency range of the spectra remains unaltered, indicating the absence of an anode surface process. Interestingly, the frequencies of the impedance spectra affected by sulfur are more than two orders of magnitude higher than the ones for cell A, indicating significant

differences between the behavior of Ni/CGO10 and Ni/CGO40-based anodes. However, the affected process is still at a frequency 2-3 orders of magnitude lower than the one for Ni/YSZ which is caused by the double layer capacitance at the interface between Ni and YSZ.[2][7] Although the peak frequency of the affected process is significantly higher for cell B than for cell A, the overall sulfur poisoning behavior remains similar both in regard to magnitude of the performance drops and their evolution in dependency of H_2S concentration and current density. Under the assumption that the resistances of both anode processes are approximately the same, the capacitance of the sulfur-affected process for the Ni/CGO40-based anode can be estimated to be twice the one of Ni/CGO10. Fig. 11 shows SEM pictures of the respective anodes. The microstructure of cell B is finer and less porous than the one of cell A. This could lead to an increased TPB length and a faster charge transfer reaction and could furthermore, be reflected by a shift of the anode charge transfer reaction to higher frequencies. However, due to the similarity of the performance with respect to the i-V curves (Fig. S2 and Fig. S4) and the polarization resistances derived from impedance measurements (e.g. Fig. 4a and Fig. 7a), we do not expect a frequency shift as high as two orders of magnitude. However, a minor influence of the different microstructures cannot be excluded.

In literature it has been shown that the amount of Ce^{3+} in CGO is affected by the Gd doping concentration as the introduction of a trivalent dopant enhances the stability of Ce^{4+}.[61] It was also reported that Gd doping higher than 25 % possibly leads to surface segregation of the Gd phase and consequently, a more tortuous Ce network within the CGO phase.[62] This is reflected by a significantly lower electronic conductivity of CGO at higher Gd contents.[61] Thus, as the capacitance of CGO is determined by the amount of available Ce^{3+}, its value can be expected to be significantly lower for CGO40 than for CGO10 entailing a substantial shift of the surface process to higher frequencies in the impedance spectra. Although similar relaxation frequencies impede the direct separation of the anode surface process, the results of equivalent circuit modeling in Table S2 confirm the significantly lower capacitance value in the case of the CGO40-based anode (~100 mF, compared to ~1 F for Ni/CGO10). This large shift in capacitance could also be interpreted to be caused by a reduced electrochemically active region on CGO40.[63]

In their ascription of the low frequency peak of Ni/CGO40 to a charge-transfer process, an important argument in the work of Iwanschitz et al. is the comparison to other experimental literature data, among them many studies based on Ni/CGO anodes with a lower Gd content.[22] Although this process was also observed in the present work as shown in Fig. 3, it is not visibly affected by sulfur exposure making a charge-transfer process as its origin unlikely. Throughout the last sections it was shown that the anode surface process observed at frequencies around 0.1 Hz in Ni/CGO10 anodes is observed at significant higher frequencies for Ni/CGO40-based anodes.

Thus, it can be concluded that impedance spectra of Ni/CGO anodes with different Gd content has to be handled with caution since processes might be subject to significant frequency shifts, which can lead to misinterpretations. The physico-chemical origin of the observed low-frequency process in Ni/CGO40 anodes and if it is also presented in Ni/CGO10-based anodes so far remains unclear. It could possibly be related to a surface diffusion process as suggested in literature.[24]

The influence of current density and temperature.

In order to compare the degradation behavior in dependency of the current density, voltage drops and ASR changes are depicted over the imposed H_2S concentrations in Fig. 8a+b. Furthermore, Fig. 8c+d show the influence of temperature. All curves show a similar characteristic saturation behavior as in Fig. 5, indicating that the underlying poisoning mechanism is probably the same. Also similar to Fig. 5, increasing current density shows a mitigation effect on the sulfur poisoning behavior which is reflected by a decreasing ASR increase with current density. In contrast to Fig. 5, even the ASR increase values for the OCV experiments obey this trend.

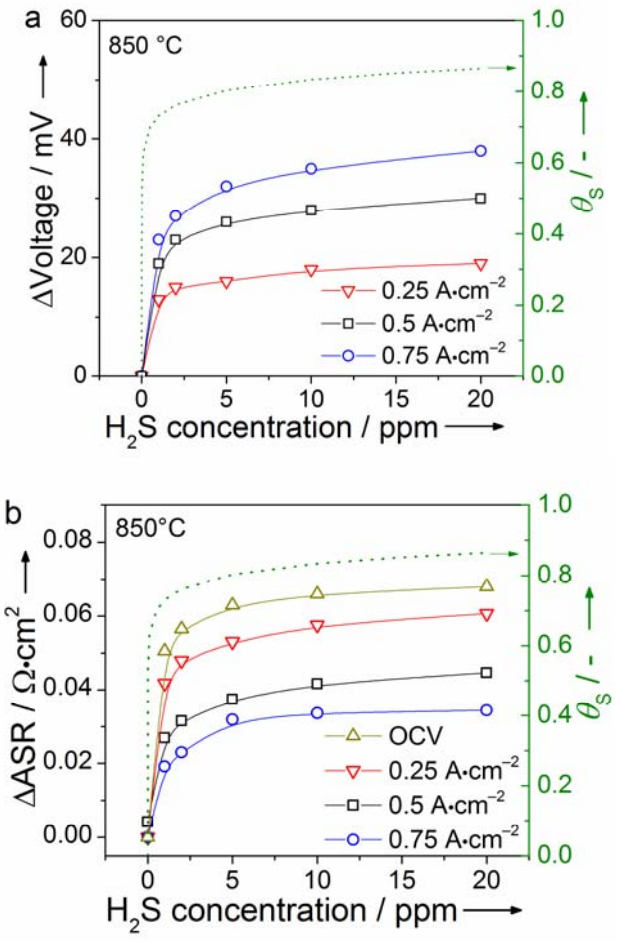

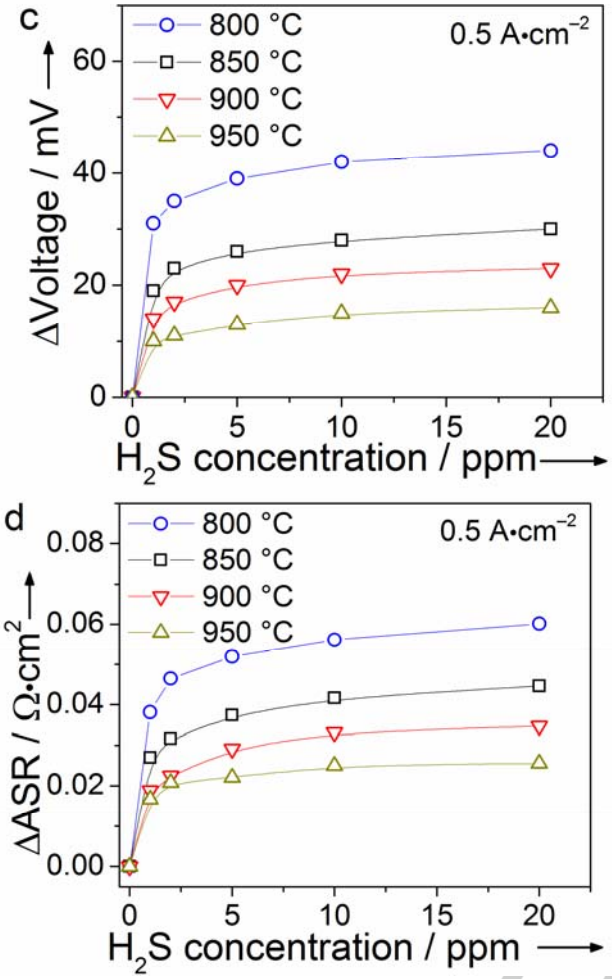

Figure 8 (a) Accumulated voltage drop and (b) accumulated ASR increase at temperature T = 850 °C, OCV, pO_2 = 0.21 atm, pH_2 = 0.97 atm, $pH2O$ = 0.03 atm, as a function of H_2S concentration at different current densities. (c) Accumulated voltage drop and (d) accumulated ASR increase at a current density of 0.5 A·cm^{-2}, OCV, pO_2 = 0.21 atm, pH_2 = 0.97 atm, pH_2O = 0.03 atm, as a function of H_2S concentration at temperatures. The right y-axes in (a) and (b) show the calculated sulfur coverage on Ni according to the Temkin isotherm derived in Ref.[54].

Both Fig. 8c and 8d show the same trend of a lower voltage drop, respectively lower ASR increase with increasing temperature analogous to the behavior of cell A shown in Fig. 7. The already mentioned increasing sulfur desorption could also occur for sulfur surface poisoning of the CGO surface as it was confirmed by a combined temperature programmed desorption (TPD) and X-ray Photoelectron Spectroscopy (XPS) analysis by Mullins et al.[35] In this study the adsorption and dissociation of hydrogen sulfide was investigated on reduced ceria surfaces that resemble gadolinia-doped ceria surface with regard to their high Ce^{3+} surface concentration showing that the sulfur coverage is decreasing with temperature. Even for temperatures as high as 700 °C the authors could detect sulfur on the reduced ceria surface. However, the authors also mention that above 500 °C sulfur could diffuse into bulk ceria, thus, lowering the surface coverage which could possibly give rise to long-term degradation effects. The incorporation of sulfur into the CGO10 bulk phase at 10 ppm H_2S exposure was also recently shown to be higher at increased temperatures by means of TOF-SIMS.[64] In the present study, by means of EDX analysis, we were not able to detected any traces of sulfur post-mortem. Thorough long-term experiments will be required in order to shed more light on the sulfur-CGO interactions in SOFC operation.

Fig. 9 confirms the behavior observed in Fig. 8, with a more pronounced increase of the imaginary impedance at higher temperatures and lower current densities. In contrast to the Ni/CGO10-based cells, however, the peak frequencies of the differential impedance spectra decrease with decreasing temperature, exhibiting the typically observed behavior for thermally activated processes. Furthermore, the change from OCV conditions to 0.75 A·cm^{-2} leads to a peak frequency shift from 23 Hz to 37 Hz which is a lot smaller than the one observed in Fig. 6. This is an indication that, in contrast to Ni/CGO10, the capacitance of the anode surface process on the Ni/CGO40-based anode is significantly less dependent on temperature and gas phase composition.

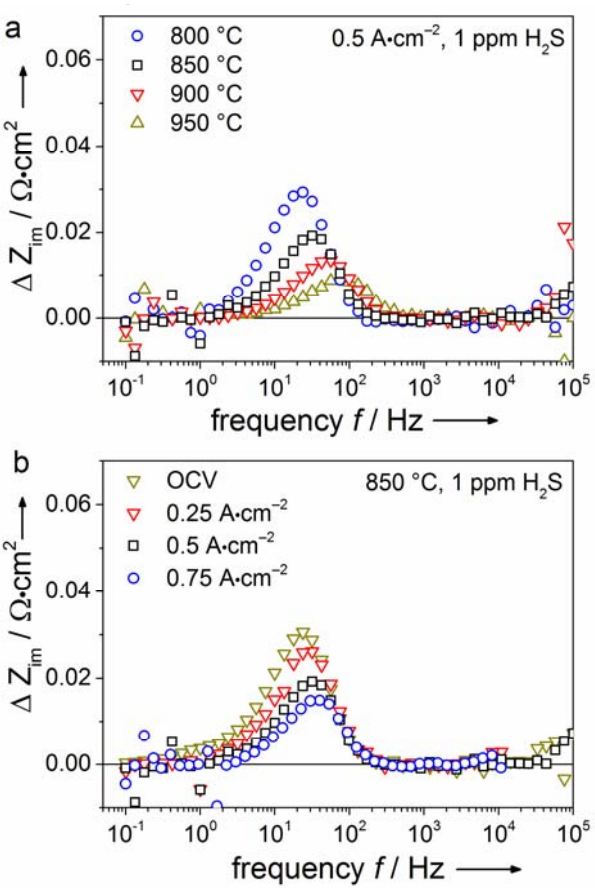

Figure 9. Differential impedance spectra (subtraction of imaginary impedance of 0 ppm H_2S spectra from 1 ppm H_2S) for a) different temperatures at constant i = 0.5 A·cm^{-2} and b) different current densities at constant T = 850 °C.

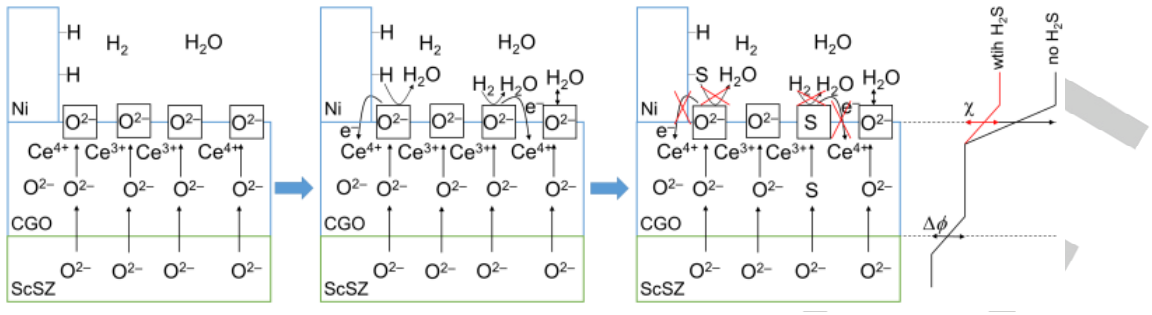

Figure 10. Schematic illustration of reaction mechanism of fuel oxidation and sulfur poisoning mechanisms in Ni/CGO-based anodes of SOFC. The first block represents the general initial configuration of Ni/CGO anodes, the second block shows the normal operation upon exposure to H_2/H_2O, the third block shows the influence of sulfur on the (electro-)chemical processes and the fourth diagram demonstrates the potentials drop at different interfaces. All structural details and scaling are exaggerated merely for illustration purposes.

The influence of H_2S on the fuel oxidation mechanism in Ni/CGO-based anodes

While early studies investigating sulfur poisoning of Ni/CGO and Ni/YSZ anodes concluded both anodes to have the same underlying sulfur poisoning mechanism, recently, the reason for the high sulfur tolerance of Ni/CGO was explained to originate from its mixed ionic and electronic conductivity (MIEC) characteristics.[8,10,11] Multiple studies have suggested that Ni primarily assumes the role of a pure electronic conductor in Ni/CGO anodes, thus improving the comparatively low electronic conductivity of CGO and extending the electrochemical reaction zone to the gas/ceria interface.[17] According to these studies, the sulfur adsorption on the Ni surface would not be expected to have a major influence on SOFC performance, which is in contrast to the sulfur poisoning behavior presented in this work. However, it was recently experimentally confirmed that pure CGO anodes can be poisoned by sulfur as well leading to the same characteristic performance drops as for Ni/CGO composite electrodes.[34] Furthermore, computational ab initio studies have shown that H_2S can dissociate on the ceria surface, creating elemental sulfur blocking the active surface area.[65] Probably, the observed sulfur poisoning of Ni/CGO anodes is a convolution of the surface poisoning of both Ni and CGO surface as illustrated in Fig. 10. Moreover, in literature sulfur atoms were observed in the CGO bulk phase, possibly indicating a mitigating effect of sulfur diffusion on the poisoning behavior.

Although the impedance spectra of Ni/CGO10 and Ni/CGO40-based anodes exhibit significant differences, the similarity of their sulfur poisoning behavior leads us to the conclusion that their underlying mechanisms are probably the same. The large differences in capacitance of the identified anode surface processes are likely to be caused by the lower availability of Ce^{3+} and thus possibly, a reduced electrochemically active region on CGO40. As it is outlined above, fuel oxidation on Ni/CGO-based anodes of SOFC proceeds essentially via the so-called bulk-surface path, where oxygen anions first migrate through the electrolyte/electrode boundary (YSZ/CGO) and then through the electrode-bulk/electrode-surface interface (CGO-bulk/CGO-surface).[28] Finally, at the surface of CGO, oxygen atoms are oxidized by hydrogen forming H_2O. Hydrogen can be dissociated on Ni and supplied to CGO by a spillover mechanism, or alternatively could be directly dissociated and oxidized on CGO. Oxidation could also occur on CGO via a Mars-van-Krevelen mechanism as it was suggested for CO oxidation on ceria catalysts.[66] While all of these mechanisms could be competitive, it is likely that the dominating mechanism depends on the microstructure of the respective electrode. This is supported by the considerable differences between the voltage drops observed in the present study and values reported in literature. As it is shown above, sulfur adsorbs both on the Ni and the CGO surface and blocks active surface sites of the electrode deteriorating fuel oxidation. As a result, the electrostatic surface potential step (χ) shown in red in Fig. 10 diminishes. The interfacial potential step ($\Delta\phi$) seems to stay constant during our experiments indicating no significant influence of sulfur on the CGO bulk-surface transport for the exposure times investigated. As both hypotheses (sulfur poisoning of Ni and CGO) are supported by a substantial amount of studies, a clear mechanistic explanation cannot be given within the framework of the present study. In order to further investigate the role of Ni during sulfur poisoning of Ni/CGO anodes, more careful electrochemical poisoning measurements on SOFC with varying composition of the metallic phase (Ni, Cu, Au) could be helpful.

Conclusions

The present work aims to advance the understanding of the electrochemical processes occurring during sulfur poisoning of Ni/CGO-based anodes. Therefore, electrolyte-supported Ni/CGO10 and Ni/CGO40-based SOFC were extensively characterized via current-voltage curves and impedance spectroscopy. Moreover, the short-time sulfur poisoning behavior of the SOFC was systematically investigated for a wide range of operating conditions with varying temperatures and current densities in H_2/H_2O fuels with different H_2S concentrations between 1 – 20 ppm. The investigated cells showed performance losses of up to 100 mV which is considerably higher than other literature studies reported demonstrating a possibly considerable effect of microstructure of Ni/CGO anodes on sulfur tolerance. The analysis of the ASR increase displayed a sulfur mitigation effect at high current loads and temperatures. The poisoning behavior was shown to be

reversible for short exposure times. The sulfur poisoning behavior of the different anodes was observed to be similar in both magnitude of cell voltage drops and saturation behavior. However, the analysis of comparable impedance spectra revealed that the sulfur-affected processes can be found at substantially different relaxation frequencies depending on the Gd-doping level of the CGO-based anode. Ni/CGO40-based anodes were affected at frequencies of approximately 50 Hz, while impedance spectra of Ni/CGO10-based anodes showed an increase at 0.1 Hz. Moreover, the capacitance of the anode surface process in Ni/CGO10 was shown to exhibit a significant dependency on both operating temperature and gas phase composition reflecting a changing Ce^{3+} concentration in CGO, while this was not the case for Ni/CGO40-based anodes. Based on these differences it could be demonstrated that the capacitance of Ni/CGO-based anodes is strongly dependent on multiple parameters and thus, a direct comparison between impedance spectra of different Ni/CGO-based anodes as it is frequently done in literature should be avoided.

While the observed reversible degradation and voltage drops are encouraging with regard to the operation of Ni/CGO anodes with sulfur-containing H_2/H_2O fuel gases, further research efforts have to be devoted to the investigation of sulfur poisoning in reformate-operated Ni/CGO-based SOFC. In order to gain a deeper understanding of the mechanism of Ni/CGO, symmetrical cell measurements on a laboratory scale have to be designed in order to avoid the convolution of anode processes with cathode and/or gas conversion processes.

Experimental Section

Two different kinds of electrolyte-supported SOFC (ESC, hereafter named as cell A and cell B) were investigated, both based on 160 µm thick Sc-stabilized zirconia electrolytes and 65 µm thick LSM/ScSZ cathodes. Cell A is a commercial SOFC with a $Ni/Ce_{0.9}Gd_{0.1}O_{2-\delta}$ (CGO10) anode manufactured by Kerafol. Cell B was produced and provided by Hexis employing a $NiCu5/Ce_{0.6}Gd_{0.4}O_{2-\delta}$ (CGO40) anode. The weight ratio between metallic and ceramic phase was 50:50 in both cases. Cell A employed 10Sc1CeSZ as material for electrolyte and the active cathode layer. The composition of the LSM was $(La_{0.75}Sr_{0.25})_{0.95}MnO_3$. The weight ratio between LSM and ScSZ in the composite electrode was 50:50. Cell B consisted of a 6ScSZ electrolyte and an $(La_{0.75}Sr_{0.25})_{0.95}MnO_3$/8YSZ cathode. Scanning electron microscopy (SEM) images of polished cross sections of the anodes of cells A (a) and B (b), both 25 µm thick, were recorded with a Zeiss Ultra Plus SEM and are shown in Fig. 11. Cell A employed an additional 5 µm thick CGO10 adhesion layer between electrolyte and functional anode layer. In cell B the functional anode layer was directly applied onto the electrolyte. Furthermore, in both cells a current collector layer with increased Ni content was utilized. The use of copper as anode material is known to entail a higher carbon and sulfur tolerance.[32] It has been reported that in Cu-ceria composite electrodes, the metal phase is simply an electronic conductor and does not play a catalytic role.[67,68] Moreover, copper only accounts for 5 wt% of the metallic phase. Thus, although minor effects on the extent of sulfur poisoning cannot be excluded, the influence of Cu on the general sulfur poisoning behavior of cell B is assumed to be negligible. In any case, also due to different processing conditions and microstructure, this work only presents a qualitative comparison of the cells. The active area of the planar cells was 4 x 4 cm^2 with a total area of 5 x 5 cm^2. Fig. S1 illustrates the experimental setup in which the cells were tested enabling the characterization of up to 4 cells simultaneously. This rather unusual configuration provides some important advantages compared to other test rigs. In particular, important parameters for fuel cell characterization, such as current density and sulfur concentration in the fuel gas can be varied simultaneously from cell to cell in the same experiment allowing the establishment of a detailed experimental map of SOFC performance and durability. The testing cells were placed in the reactive chamber (ceramic cell housing) as illustrated in Fig. S1b, where the anode and the cathode were contacted with nickel and platinum meshes, respectively, employing gold as the sealant between the anode and the cathode side. In addition, thermocouples (TC) were positioned just next to the respective electrode in the center of the channel rib. If not stated otherwise, the cells were operated with varying H_2/H_2O fuel mixtures and different H_2S concentrations at a constant total fuel flow rate of 1 l•min^{-1} for each cell. The cathode was operated with air with a constant flow rate of 2 l•min^{-1}. Humidification was carried out by running the gas through a temperature-controlled water bubbler. H_2S was taken from a pressurized H_2S/H_2 bottle containing 100 ppm H_2S. In order to avoid sulfur adsorption on the piping and its dissolution in the water bubbler, the sulfur was injected into the fuel stream only 6 cm away from the cell housing and, furthermore, Teflon-coated tubing was used. The cells were briefly heated (3 K/min) to 950 °C for sealing and subsequently reduced at 900 °C. Then, an initial cell characterization was carried out comprising cell voltage curves as a function of current density (*i-V* curves) and electrochemical impedance spectra (EIS) at different temperatures and a series of different gas compositions fed to the anode and cathode, respectively. The *i-V* curves and impedance spectra were measured between 650 °C and 950 °C (800 °C – 950 °C for cell B) at steps of 50 K and pH_2/pH_2O (97/3) mixtures. Furthermore, impedance spectra were recorded at different pH_2O between 0.03 and 0.5 atm. Subsequently, the temperature was set to 850 °C where sulfur poisoning experiments were conducted for different current densities. The investigated current densities were 0.5 A·cm^{-2}, 0.75 A·cm^{-2}, 0.25 A·cm^{-2}, and open circuit voltage (OCV), in this order. In addition, subsequently, the operating temperature was varied to 900 °C, 950 °C (only for cell B) and 800 °C where poisoning experiments were performed at 0.5 A·cm^{-2}. For cell A, the poisoning experiments for 800 °C and 900 °C were carried out with a different cell of same specifications from the same batch. Also the experiment at 850 °C with 0.5 A·cm^{-2} was repeated with this cell. The poisoning experiments were carried out for a H_2/H_2O ratio of 97/3. For a systematic investigation of the sulfur poisoning behavior the H_2S concentration was stepwise increased and set to 1, 2, 5, 10, and 20 ppm at each operating point until saturation occurred. After saturation of the last performance drop related to 20 ppm H_2S, its supply was switched off, the gas flow was substituted with pure H_2 and the anode was regenerated until full recovery of the SOFC performance was achieved. If not mentioned otherwise, the cells were characterized by electrochemical impedance spectroscopy by means of an electrochemical workstation (Zahner® PP-240 with Thales software) in a frequency range from 100 mHz to 100 kHz with 8 points/decade. The amplitude of the current stimulus was chosen in order to achieve a voltage response not higher than 15 mV. The distribution of relaxation times (DRT) was calculated with a modified Levenberg-Marquardt algorithm adapted from Ref.[69]

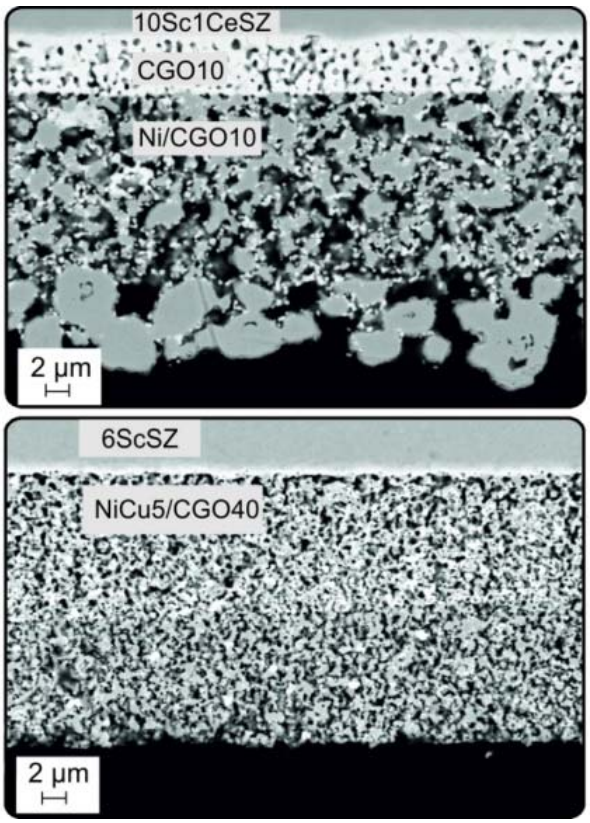

Figure 11. Scanning electron microscopy cross section image of the anodes of reference cells A (upper picture) and B (lower picture).

Acknowledgements

We gratefully acknowledge financial support from the German Ministry of Education and Research (BMBF) within the framework of the project "SOFC-Degradation: Analyse der Ursachen und Entwicklung von Gegenmaßnahmen" via grant number 03SF0494C. Furthermore, the authors would like to thank Dr. Andreas Mai from Hexis for the generous supply of cells. The authors are deeply grateful to Michael Hoerlein for help regarding test bench setup, cell testing and numerous scientific discussions. Dr. Aziz Nechache is acknowledged for helpful discussions. We would also like to thank Miriam Steinhauer for help with the calculation of the DRT.

Keywords: • catalysis • ceria • electrochemistry • impedance spectroscopy • Ni/GDC

References

[1] R. Kee, H. Zhu, *Combust. Sci. Technol.* **2008**, *180*, 1207.
[2] M. Riegraf, G. Schiller, R. Costa, K. Andreas Friedrich, A. Latz, V. Yurkiv, *J. Electrochem. Soc.* **2015**, *162*, F65.
[3] A. Hagen, J. F. B. Rasmussen, K. Thydén, *J. Power Sources* **2011**, *196*, 7271.
[4] A. Hauch, A. Hagen, J. Hjelm, T. Ramos, *J. Electrochem. Soc.* **2014**, *161*, F734.
[5] A. Hagen, G. B. Johnson, P. Hjalmarsson, *J. Power Sources* **2014**, *272*, 776.
[6] A. Weber, S. Dierickx, A. Kromp, E. Ivers-Tiffée, *Fuel Cells* **2013**, *13*, 487.
[7] M. Riegraf, V. Yurkiv, G. Schiller, R. Costa, A. Latz, K. A. Friedrich, *J. Electrochem. Soc.* **2015**, *162*, 1324.
[8] S. Kavurucu Schubert, M. Kusnezoff, A. Michaelis, S. I. Bredikhin, *J. Power Sources* **2012**, *217*, 364.
[9] J. P. Trembly, A. I. Marquez, T. R. Ohrn, D. J. Bayless, *J. Power Sources* **2006**, *158*, 263.
[10] J. P. Ouweltjes, P. V. Aravind, N. Woudstra, G. Rietveld, *J. Fuel Cell Sci. Technol.* **2006**, *3*, 495.
[11] P. V. Aravind, J. P. Ouweltjes, N. Woudstra, G. Rietveld, *Electrochem. Solid-State Lett.* **2008**, *11*, B24.
[12] C. Xu, P. Gansor, J. W. Zondlo, K. Sabolsky, E. M. Sabolsky, *J. Electrochem. Soc.* **2011**, *158*, B1405.
[13] L. Zhang, S. P. Jiang, H. Q. He, X. Chen, J. Ma, X. C. Song, *Int. J. Hydrogen Energy* **2010**, *35*, 12359.
[14] E. Brightman, D. G. Ivey, D. J. L. Brett, N. P. Brandon, *J. Power Sources* **2011**, *196*, 7182.
[15] P. Lohsoontorn, D. J. L. Brett, N. P. Brandon, *J. Power Sources* **2008**, *183*, 232.
[16] C. Zhang, M. E. Grass, A. H. McDaniel, S. C. DeCaluwe, F. El Gabaly, Z. Liu, K. F. McCarty, R. L. Farrow, M. A. Linne, Z. Hussain, G. S. Jackson, H. Bluhm, B. W. Eichhorn, *Nat. Mater.* **2010**, *9*, 944.
[17] W. C. Chueh, Y. Hao, W. Jung, S. M. Haile, *Nat. Mater.* **2011**, *11*, 155.
[18] W. C. Chueh, S. M. Haile, *Phys. Chem. Chem. Phys.* **2009**, *11*, 8144.
[19] Z. A. Feng, F. El Gabaly, X. Ye, Z.-X. Shen, W. C. Chueh, *Nat. Commun.* **2014**, *5*, 1.
[20] S. C. Decaluwe, M. E. Grass, C. Zhang, F. El Gabaly, H. Bluhm, Z. Liu, G. S. Jackson, A. H. McDaniel, K. F. McCarty, R. L. Farrow, M. A. Linne, Z. Hussain, B. W. Eichhorn, *J. Phys. Chem. C* **2010**, *114*, 19853.
[21] T. Nakamura, T. Kobayashi, K. Yashiro, A. Kaimai, T. Otake, K. Sato, J. Mizusaki, T. Kawada, *J. Electrochem. Soc.* **2008**, *155*, B563.
[22] B. Iwanschitz, J. Sfeir, A. Mai, M. Schütze, *J. Electrochem. Soc.* **2010**, *157*, B269.
[23] V. Papaefthimiou, M. Shishkin, D. K. Niakolas, M. Athanasiou, Y. T. Law, R. Arrigo, D. Teschner, M. Hävecker, A. Knop-Gericke, R. Schlögl, T. Ziegler, S. G. Neophytides, S. Zafeiratos, *Adv. Energy Mater.* **2013**, *3*, 762.
[24] S. Primdahl, M. Mogensen, *Solid State Ionics* **2002**, *152*, 597.
[25] S. Primdahl, Y. L. Liu, *J. Electrochem. Soc.* **2002**, *149*, A1466.
[26] M. Chen, B. H. Kim, Q. Xu, B. G. Ahn, D. P. Huang, *Solid State Ionics* **2010**, *181*, 1119.
[27] P. Kim, D. J. L. Brett, N. P. Brandon, *J. Power Sources* **2009**, *189*, 1060.
[28] W. C. Chueh, S. M. Haile, *Annu. Rev. Chem. Biomol. Eng.* **2012**, *3*, 313.
[29] J. Fleig, *Phys. Chem. Chem. Phys.* **2005**, *7*, 2027.
[30] V. Yurkiv, R. Costa, Z. Ilhan, A. Ansar, W. G. Bessler, *J. Electrochem. Soc.* **2014**, *161*, F480.
[31] H. Kishimoto, K. Yamaji, T. Horita, Y.-P. Xiong, *Electrochemistry* **2009**.
[32] H. He, R. J. Gorte, J. M. Vohs, *Electrochem. Solid-State Lett.* **2005**, *8*, A279.
[33] P. Lohsoontorn, D. J. L. Brett, N. P. Brandon, *J. Power Sources* **2008**, *175*, 60.
[34] B. Mirfakhraei, S. Paulson, V. Thangadurai, V. Birss, *J. Power Sources* **2013**, *243*, 95.
[35] D. R. Mullins, T. S. McDonald, *Surf. Sci.* **2007**, *601*, 4931.
[36] W. G. Bessler, S. Gewies, *J. Electrochem. Soc.* **2007**, *154*, B548.
[37] S. Primdahl, *J. Electrochem. Soc.* **1999**, *146*, 2827.
[38] S. Gewies, W. G. Bessler, *J. Electrochem. Soc.* **2008**, *155*, B937.
[39] A. Babaei, S. P. Jiang, J. Li, *J. Electrochem. Soc.* **2009**, *156*, B1022.
[40] R. Barfod, M. Mogensen, T. Klemenso, A. Hagen, Y.-L. Liu, P. Vang Hendriksen, *J. Electrochem. Soc.* **2007**, *154*, B371.
[41] M. Kornely, A. Neumann, N. H. Menzler, A. Leonide, A. Weber, E. Ivers-Tiffée, *J. Power Sources* **2011**, *196*, 7203.
[42] Y. Tao, S. D. Ebbesen, M. B. Mogensen, *J. Electrochem. Soc.* **2014**, *161*, F337.
[43] M. Vogler, A. Bieberle-Hütter, L. Gauckler, J. Warnatz, W. G. Bessler, *J. Electrochem. Soc.* **2009**, *156*, B663.
[44] L. Jia, X. Wang, B. Hua, W. Li, B. Chi, J. Pu, S. Yuan, L. Jian, *Int. J. Hydrogen Energy* **2012**, *37*, 11941–11945.
[45] W. An, D. Gatewood, B. Dunlap, C. H. Turner, *J. Power Sources* **2011**, *196*, 4724–4728.
[46] A. Hagen, *J. Electrochem. Soc.* **2013**, *160*, F111.
[47] W. C. Chueh, W. Lai, S. M. Haile, *Solid State Ionics* **2008**, *179*, 1036.
[48] S. B. Adler, J. A. Lane, B. C. H. Steele, *J. Electrochem. Soc.* **1996**, *143*, 3554.
[49] C. Graves, C. Chatzichristodoulou, M. B. Mogensen, *Faraday*

Discuss. **2015**, *182*, 75.
[50] Z. Cheng, S. Zha, M. Liu, *J. Power Sources* **2007**, *172*, 688.
[51] Z. Cheng, J.-H. Wang, Y. Choi, L. Yang, M. C. Lin, M. Liu, *Energy Environ. Sci.* **2011**, *4*, 4380.
[52] J. F. B. Rasmussen, A. Hagen, *J. Power Sources* **2009**, *191*, 534.
[53] K. Sasaki, K. Susuki, A. Iyoshi, M. Uchimura, N. Imamura, H. Kusaba, Y. Teraoka, H. Fuchino, K. Tsujimoto, Y. Uchida, N. Jingo, *J. Electrochem. Soc.* **2006**, *153*, A2023.
[54] I. Alstrup, J. Rostrup-Nielsen, S. Røen, *Appl. Catal.* **1981**, *1*, 303.
[55] D.-H. Lim, H. S. Kim, S. P. Yoon, J. Han, C. W. Yoon, S. H. Choi, S. W. Nam, H. C. Ham, *Phys. Chem. Chem. Phys.* **2014**, *16*, 10727.
[56] Y. Matsuzaki, I. Yasuda, *Solid State Ionics* **2000**, *132*, 261.
[57] A. Leonide, V. Sonn, A. Weber, E. Ivers-Tiffée, *J. Electrochem. Soc.* **2008**, *155*, B36.
[58] M. G. H. M. Hendriks, J. E. Ten Elshof, H. J. M. Bouwmeester, H. Verweij, *Solid State Ionics* **2002**, *146*, 211.
[59] M. Vogler, A. Bieberle-Hütter, L. Gauckler, J. Warnatz, W. G. Bessler, *J. Electrochem. Soc.* **2009**, *156*, B663.
[60] W. C. Chueh, A. H. McDaniel, M. E. Grass, Y. Hao, N. Jabeen, Z. Liu, S. M. Haile, K. F. McCarty, H. Bluhm, F. El Gabaly, *Chem. Mater.* **2012**, *24*, 1876.
[61] M. Mogensen, *J. Electrochem. Soc.* **1994**, *141*, 2122.
[62] Z. Li, T. Mori, G. J. Auchterlonie, J. Zou, J. Drennan, Z. Li, T. Mori, G. J. Auchterlonie, J. Zou, **2014**, *093104*, 13.
[63] J. Fleig, *J. Power Sources* **2002**, *105*, 228.
[64] M. Gerstl, A. Nenning, R. Iskandar, V. Rojek-Wöckner, M. Bram, H. Hutter, A. Opitz, *Materials (Basel).* **2016**, *9*, 649.
[65] D. Marrocchelli, B. Yildiz, *J. Phys. Chem. A* **2011**, *2*, 2411.
[66] E. Aneggi, J. Llorca, M. Boaro, A. Trovarelli, *J. Catal.* **2005**, *234*, 88.
[67] C. Lu, W. L. Worrell, J. M. Vohs, R. J. Gorte, *J. Electrochem. Soc.* **2003**, *150*, A1357.
[68] M. Miyake, S. Matsumoto, M. Iwami, S. Nishimoto, Y. Kameshima, *Int. J. Hydrogen Energy* **2016**, *1*, 2–8.
[69] S. Risse, N. A. Cañas, N. Wagner, E. Härk, M. Ballauff, K. A. Friedrich, *J. Power Sources* **2016**, *323*, 107.

WILEY-VCH